

Axion-plasmon-polariton hybridization in a graphene periodic structure

Daqing Liu¹, Xiuqin Hua¹, Dong Sun¹, Xingfang Jiang¹ and Xiang Zhao²

¹ *School of Microelectronics and Control Engineering, Changzhou University, Changzhou, 213164, China*

² *School of Science, Xi'an Jiaotong University, Xi'an, 710049, China*

Abstract

This study investigated the hybridization between an axion and plasmon polariton, attributed to the coupling achieved by combining modified electrodynamics and hydrodynamic approaches on a plasmon-polariton in a graphene periodic structure. The enhancement of the effective coupling was also studied. Furthermore, corrections for the axion and the lowest plasmon-polariton hybridization state spectra have been presented. An observable was proposed to detect axions, which is significant even when the effective coupling is not large, especially as the axion mass decreases. The study shows that the resulting structure provides a sensitive and wide-mass-spectrum platform for detecting axions at the sub-meV scale.

Keywords: axion, plasmon polariton, graphene, hybridization.

1 Introduction

An axion was originally postulated to address the strong charge-parity problem^[1,2]. It is considered that this hypothetical particle has an extremely small mass (possibly smaller than meV, for instance, in the range of $10^{-3} - 1$ meV) and couples very weakly with quarks, leptons, and photons (the coupling between the axion and common matters was implied as $g \leq 10^{-10} \text{GeV}^{-1}$). This particle was considered to be one of the prime dark matter candidates^[3-9]. Recently, dark-matter axion detection emerged as a promising research field^[10-19], and many studies have used a variety of techniques to detect axions^[20-27].

Several studies^[16,17,19] have used the interactions between axions and plasma to detect axions using photoelectric techniques^[9,20,27]. However, when using such an approach, it is challenging to control the parameters. In this study, we propose a novel scheme to observe the axion effect in a laboratory. In the presence of strong background magnetic fields, the coupling between an axion and plasmon polariton (PP), which is not plasma but a collective excited state in a material, occurs in a graphene periodic structure. We show that the effective coupling between an axion and PP can be enhanced by adjusting certain parameters, such as Fermi energy, the background magnetic field, and graphene interlayer distances. Corrections to the plasmon-polariton/axion hybridization state spectra were presented and an observable to detect axion was suggested subsequently. The signal is significant even when the effective coupling is not large, especially as the axion mass decreases. Furthermore, as the significance does not rely on the phenomenon of resonance, there is a broad detectable range of axion mass spectrum using the observable. The proposed method therefore provides an effective platform for detecting axion particles.

2 Modified electromagnetism in a graphene structure

A three-dimensional periodic structure of graphene layers embedded in a medium with permittivity ϵ (we set ϵ to be equal to vacuum permittivity ϵ_0) is shown in Fig. 1. The graphene layers parallel to the plane defined by $z = 0$ are assumed to be infinite for simplification. The distance between the layers is represented as d . Each

graphene layer is N -doped and has an equal Fermi energy, $E_F > 0$, with $n_0 = \frac{k_F^2}{\pi} = \frac{E_F^2}{\pi \hbar^2 v_F^2}$ where $\hbar k_F$, v_F , and n_0 are Fermi momentum, Fermi velocity (1×10^6 m/s) and two-dimensional (2D) carrier equilibrium density, respectively. Considering the graphene carrier as a 2D electron gas, the hydrodynamic equation of the carrier is expressed as follows [28]

$$m_g n \frac{\partial \mathbf{v}}{\partial t} + m_g n (\mathbf{v} \cdot \nabla) \mathbf{v} = -en(\mathbf{E} + \mathbf{v} \times \mathbf{B}) - \nabla P, \quad (1)$$

where $m_g = \hbar k_F / v_F$ is the effective mass of carriers at the Fermi surface [28, 29], which is at the order of $0.1 - 1$ eV and can be tuned by E_F , and $P = \frac{\hbar v_F}{3\pi} (\pi n)^{3/2}$ ($\nabla P = \frac{\hbar v_F}{2} \sqrt{\pi n} \nabla n$) is the carrier pressure in the graphene.

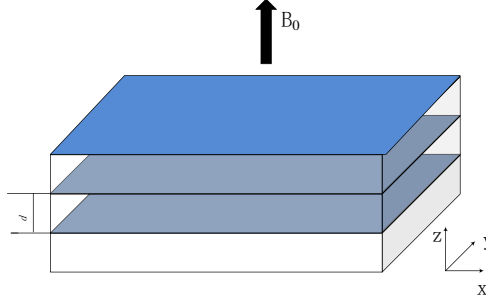


Figure 1: Three-dimensional periodic structure of graphene ribbons embedded in the medium.

The continuity equation is

$$\frac{\partial n}{\partial t} + \nabla \cdot (n\mathbf{v}) = 0. \quad (2)$$

When d is small enough (compared to the axion scale), the modified Maxwell equations become:

$$\begin{cases} \nabla \cdot \mathbf{E} = -e\rho/\epsilon_0 + cg\nabla\phi \cdot \mathbf{B}, \\ \nabla \times \mathbf{B} = \frac{\partial \mathbf{E}}{c^2 \partial t} + \mu \mathbf{j}/d + \frac{g}{c} (\mathbf{E} \times \nabla\phi - \mathbf{B} \frac{\partial \phi}{\partial t}), \\ \nabla \cdot \mathbf{B} = 0, \\ \nabla \times \mathbf{E} = -\frac{\partial \mathbf{B}}{\partial t}, \end{cases} \quad (3)$$

where $\rho = (n - n_i)/d = (n - n_0)/d$ is the three-dimensional (3D) particle density; μ is the vacuum permeability; \mathbf{j} is the linear current density; ϕ is the axion field; and g is the coupling between the axion and electromagnetic fields with the dimension $[M^{-1/2} T^{1/2}]$. Here, we assume that d is sufficiently small such that the boundary conditions at each graphene layer can be ignored. Unlike the traditional method [28], our hydrodynamic approach does not use the potential conception.

The Klein-Gordon equation for the axion field is:

$$\frac{\partial^2 \phi}{c^2 \partial t^2} - \nabla^2 \phi + \frac{m_\phi^2 c^2}{\hbar^2} \phi = -g\epsilon_0 \mathbf{E} \cdot \mathbf{B}, \quad (4)$$

where m_ϕ is the axion mass.

Subsequently, we cast a strong homogeneous background magnetic field, B_0 , perpendicular to graphene layers. To study the system behavior, we firstly linearize the above equations as follows:

$$\frac{\partial \mathbf{v}}{\partial t} = -\frac{e}{m_g}(\mathbf{E}_{\parallel} + \mathbf{v} \times \mathbf{B}_0) - \frac{\pi \hbar^2}{2m_g^2} \nabla n_1, \quad (5)$$

$$\frac{\partial n_1}{\partial t} + n_0 \nabla \cdot \mathbf{v} = 0, \quad (6)$$

$$\begin{cases} \nabla \cdot \mathbf{E} = -en_1/(d\epsilon_0) + cg\nabla\phi \cdot \mathbf{B}_0, \\ \nabla \times \mathbf{B} = \frac{\partial \mathbf{E}}{c^2 \partial t} + \mu \mathbf{j}/d - \frac{g}{c} \mathbf{B}_0 \frac{\partial \phi}{\partial t}, \\ \nabla \cdot \mathbf{B} = 0, \\ \nabla \times \mathbf{E} = -\frac{\partial \mathbf{B}}{\partial t}, \end{cases} \quad (7)$$

$$\frac{\partial^2 \phi}{c^2 \partial^2 t^2} - \nabla^2 \phi + \frac{m_\phi^2 c^2}{\hbar^2} \phi = -g\epsilon_0 \mathbf{E} \cdot \mathbf{B}_0, \quad (8)$$

where $n_1 = n - n_0$. In the above equations \mathbf{v} and \mathbf{j} have only x and y components, and \mathbf{E}_{\parallel} is the projection of \mathbf{E} in the xy -plane. In physics, the electrostatic perturbation along the background magnetic field will produce the axion field through Eq. (8). Then, the axion field, acting as a source, will generate the electromagnetic field according to the modified Maxwell equation (Eq. (7)). The electromagnetic field will drive the carrier oscillation, the plasmon polariton, in graphene layers according to Eq. (5). The above process is reversible. Therefore, axion-plasmon-polariton resonance occurs and axion-plasmon-polariton hybridization states exist in the structure.

We assume that the hybridization states propagate in the xz plane with the wave number $\mathbf{q} = (q \sin \theta, 0, q \cos \theta)$, and angular frequency ω , where θ is the angle between the direction of the axion propagation and the background magnetic field. Moreover, all the variables have the form $e^{i\mathbf{q} \cdot \mathbf{r} - i\omega t}$. The modified Helmholtz equations in the system transform into:

$$\kappa^2 \mathbf{B} = -\frac{g\omega}{c} \phi \mathbf{q} \times \mathbf{B}_0 + i\mu \mathbf{q} \times \mathbf{j}/d, \quad (9)$$

for the magnetic field, and

$$\kappa^2 \mathbf{E} = i\frac{en_1}{d\epsilon_0} \mathbf{q} + cg\phi(\mathbf{q} \cdot \mathbf{B}_0)\mathbf{q} + i\omega\mu \mathbf{j}/d - \frac{g\omega^2}{c} \phi \mathbf{B}_0, \quad (10)$$

for the electric field, where $\kappa^2 = q^2 - \frac{\omega^2}{c^2}$.

Decomposing all the fields into transverse and longitudinal parts, for instance, $\mathbf{E}_L = \hat{q}\hat{q} \cdot \mathbf{E} = E_L \hat{q}$ and $\mathbf{E}_T = \mathbf{E} - \mathbf{E}_L$, we have

$$\begin{aligned} \kappa^2 D_L &= i\omega\mu j_L/d + i\frac{eqn_1}{d\epsilon_0}, \\ \kappa^2 \mathbf{D}_T &= i\omega\mu \mathbf{j}_T/d - cgq^2 \phi \mathbf{B}_{0T}, \end{aligned} \quad (11)$$

where $\mathbf{D} = \mathbf{E} - cg\phi \mathbf{B}_0$. It seems that the longitudinal mode decouples with the axion field, as shown in the first equation in Eq. (11). However, the linear current density has x and y components only, and it usually has both longitudinal and transverse parts unless the hybridization states propagate along the z -axis. This is one of the crucial differences between the graphene structure and ordinary plasma.

3 Dispersion of axion-plasmon-polariton hybridization state

To obtain the dispersion of the hybridization state, \mathbf{j} , \mathbf{v} , and \mathbf{E} should be eliminated from the above equations. For linear current density, we ignore the interband contribution and write the equation as

$$\mathbf{j} = -en_0 \mathbf{v}. \quad (12)$$

We finally obtained:

$$\begin{aligned} \frac{igm_g \omega_c q \cos \theta}{d\kappa^2} n_1 + [\kappa^2 + \frac{\omega_\phi^2}{c^2} + \frac{g^2 m_g^2 \omega_c^2 c \epsilon_0}{e^2 \kappa^2} (q^2 \cos^2 \theta - \frac{\omega^2}{c^2})] \phi &= 0, \\ \frac{igdm_g c^3 q^3 \omega_p^2 \omega_c \epsilon_0 \hbar_1 \cos \theta \sin^2 \theta}{e^2 f_1} \phi + [1 - \frac{c^2 q^2 (2\omega_p^2 + v_F^2 \kappa^2) \hbar_1 \sin^2 \theta}{2f_1}] n_1 &= 0 \end{aligned} \quad (13)$$

where $h_1 = \omega_p^2 + c^2\kappa^2$, $f_1 = \omega^2 h_1^2 - c^4 \omega_c^2 \kappa^4$, $\omega_\phi = \frac{m_\phi c^2}{\hbar^2}$, $\omega_c = \frac{eB_0}{m_g}$ is the carrier cyclotron frequency at the Fermi surface, and $\omega_p^2 = \frac{e^2 n_0}{d\epsilon_0 m_g}$ is the plasmon frequency related to carrier density n_0/d and carrier effective mass m_g .

To understand the physics behind the above equations, we first set $g = 0$, that is, no coupling exists between the axion and electromagnetic fields. The first equation in (13) shows the free axion field dispersion, $\kappa^2 + \frac{m_\phi^2 c^2}{\hbar^2} = 0$, as expected. The second equation in (13) presents the results of PP dispersion, given by

$$1 - \frac{q_0^2(1 + q_0^2 - \omega_0^2) \sin^2 \theta (2 + v_{F0}^2(q_0^2 - \omega_0^2))}{2[\omega_0^2(1 + q_0^2 - \omega_0^2)^2 - \omega_{c0}^2(q_0^2 - \omega_0^2)^2]} = 0, \quad (14)$$

where the following dimensionless quantities have been introduced, $\omega_0 = \omega/\omega_p$, $\omega_{c0} = \omega_c/\omega_p$, $v_{F0} = v_F/c$, and $q_0 = cq/\omega_p$.

If we turn off the background magnetic field, that is, $\omega_{c0} = 0$, the two solutions can be expressed as:

$$\begin{aligned} (\omega/\omega_p)^2 &= \frac{1}{4} [2 + 2q_0^2 + q_0^2 v_{F0}^2 \sin^2 \theta \pm \sqrt{(2 + 2q_0^2 + q_0^2 v_{F0}^2 \sin^2 \theta)^2 - 8q_0^2(2 + q_0^2 v_{F0}^2) \sin^2 \theta}] \\ &\simeq \frac{1}{2} [1 + q_0^2 \pm \sqrt{(1 + q_0^2)^2 - 4q_0^2 \sin^2 \theta}], \end{aligned} \quad (15)$$

where $o(v_F^2/c^2)$ has been ignored. In the long-wave limit, *i.e.*, $cq \ll \omega_p$ or $q_0 \ll 1$, we have two branches: an optical branch, the dispersion of which is $\omega_{o0}^2 \equiv (\frac{\omega_o}{\omega_p})^2 = 1 + q_0^2 - \frac{q_0^2 \sin^2 \theta}{1 + q_0^2}$, and an acoustic branch, wherein $\omega_{a0}^2 \equiv (\frac{\omega_a}{\omega_p})^2 \simeq \frac{q_0^2 \sin^2 \theta}{1 + q_0^2}$.

However B_0 can not be always ignored. To illustrate the conclusion, we consider the orders of ω_p and ω_c . $\omega_c = \frac{eB_0}{m_g} = \frac{B_0 v_F^2}{E_F (eV)} \sim 10^{13} (\text{rad/s})$ (or $\hbar\omega_c \sim 10 \text{meV}$) if $B_0 \sim 1 \text{T}$ and $E_F \sim 0.1 \text{eV}$. $\omega_p = (\frac{e^2 n_0}{d\epsilon_0 m_g})^{1/2} = (\frac{e^3 E_F (eV)}{d\pi\epsilon_0 \hbar^2})^{1/2} \sim 3.7 \times 10^{11} (\text{rad/s})$ (or $\hbar\omega_p \sim 0.2 \text{meV}$) if we also set $d \sim 1 \text{cm}$. In other words, we can choose parameters to yield $\hbar\omega_p \ll \hbar\omega_c$. We can tune ω_p and ω_c by controlling E_F . For instance, when E_F decreases, ω_p also decreases but ω_c increases. For the case $\omega_{c0} \neq 0$, another branch was observed, ω_h , which was nominated as the high mode here, exhibiting an asymptotic behavior: $\omega_{h0}^2 \rightarrow 1 + q_0^2$ when $\omega_{c0} \rightarrow 0$ and $v_{F0} = 0$.

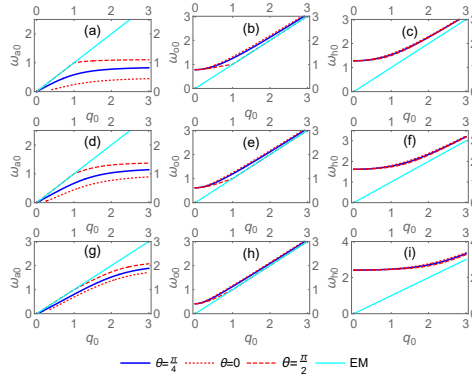


Figure 2: Dispersions of ω_a (a,d,g), ω_o (b,e,h), and ω_h (c,f,i) at different angle. We set ω_{c0} to be 0.5(a,b,c), 1.0(d,e,f), and 2.0(g,h,i) respectively. Here the symbol "EM" stands for the dispersion of electromagnetic radiation in the vacuum.

The discussions on the PP in such a structure are not sufficient, particularly when a background magnetic field exists. It is necessary to consider the influence of the background magnetic field on the PP. Neglecting $o(v_F^2/c^2)$ terms, we obtained dispersions of ω_a , ω_o , and ω_h at $\theta = 0, \frac{\pi}{4}, \frac{\pi}{2}$ and $\omega_{c0} = 0.5, 1, 2$ in Fig. 2, respectively.

From Fig. 2, we briefly list certain results based on the structure in the presence of the background magnetic field:

1. When $\theta = \frac{\pi}{2}$, implying that the PP propagates along graphene layers, in the long-wave limit, $\omega_{a0} \simeq q_0$ but $\omega_{a0} < q_0$. In other words, in the long-wave limit, the dispersion of the acoustic branch is approximately equal to that of electromagnetic (EM) radiation in the medium, as highlighted in previous studies. The statement holds in the presence of B_0 . However, the stronger the background magnetic field, the narrower the scope of the statement, as shown in 2(a), 2(d), and 2(g).
2. Generally, the larger the value of $\sin \theta$, the higher the frequency of the acoustic mode for the fixed q_0 . In particular, in the absence of B_0 , $\omega_{a0} \propto |\sin \theta|$, which was confirmed in [30]. However, as B_0 increases, the angular dependence becomes weaker, as shown in 2(a), 2(d), and 2(g).
3. In addition to ω_a , two other modes exist, ω_o and ω_h , which have frequently been ignored. The modes are angular insensitive. The dispersion of ω_h is almost isotropic. Similarly, the angular dependence becomes weaker as B_0 increases.
4. With an increase in B_0 , ω_h increases, whereas ω_o decreases. In other words, the gap between the two dispersion curves becomes larger with an increasing B_0 because $\omega_o < \omega_h$ for certain q_0 .
5. The ω_a dispersion curve is below the EM radiation curve. ω_h and ω_o curves are above the EM curve for small values of B_0 . If B_0 is sufficiently strong, *i.e.* ω_{c0} is adequately high, the ω_o and EM curves will intersect.

To consider the coupling between the axion field and PP, we further introduce dimensionless quantities, $n_{10} = \frac{c^2}{\omega_p^2} n_1$, $d_0 = \frac{\omega_p}{c} d$, $g_0 = \frac{\sqrt{\hbar} \omega_p}{c} g$, $\phi_0 = \frac{c}{\sqrt{\hbar} \omega_p} \phi$, and $\omega_{g0} = \frac{m_g c^2}{\omega_p \hbar}$. Eqs. (13) can then be written as

$$\begin{aligned} & [(q_0^2 - \omega_0^2 + \omega_{\phi 0}^2) + g_n^2 \frac{q_0^2 \cos^2 \theta - \omega_0^2}{q_0^2 - \omega_0^2}] \phi_0 + \frac{i g_n q_0 \sqrt{\pi} \cos \theta}{\sqrt{d_0 \omega_{g0} v_{F0} (q_0^2 - \omega_0^2)}} n_{10} = 0 \\ & \frac{i g_n q_0^3 v_{F0} \sqrt{\omega_{g0} d_0} (1 + q_0^2 - \omega_0^2) \cos \theta \sin^2 \theta}{\sqrt{\pi} [\omega_0^2 (1 + q_0^2 - \omega_0^2)^2 - (q_0^2 - \omega_0^2)^2 \omega_{c0}^2]} \phi_0 + [1 - \frac{q_0^2 (1 + q_0^2 - \omega_0^2) (2 + v_{F0}^2 (q_0^2 - \omega_0^2)) \sin^2 \theta}{2 [\omega_0^2 (1 + q_0^2 - \omega_0^2)^2 - (q_0^2 - \omega_0^2)^2 \omega_{c0}^2]}] n_{10} = 0 \end{aligned} \quad (16)$$

where $g_n = g_0 A_m$ with the enlargement factor $A_m = \frac{\omega_{c0} \omega_{g0}^{3/2} v_{F0}}{\sqrt{\pi} d_0}$.

Rescaling n_{10} , we can rewrite the above equation as:

$$\begin{pmatrix} (q_0^2 - \omega_0^2 + \omega_{\phi 0}^2) + g_n^2 \frac{q_0^2 \cos^2 \theta - \omega_0^2}{q_0^2 - \omega_0^2} & i g_n q_0^2 \cos \theta \sin \theta \sqrt{\frac{(q_0^2 - \omega_0^2)(1 + q_0^2 - \omega_0^2)}{\omega_{c0}^2 (q_0^2 - \omega_0^2)^2 - \omega_0^2 (1 + q_0^2 - \omega_0^2)^2}} \\ -i \frac{g_n q_0^2 \cos \theta \sin \theta}{q_0^2 - \omega_0^2} \sqrt{\frac{(q_0^2 - \omega_0^2)(1 + q_0^2 - \omega_0^2)}{\omega_{c0}^2 (q_0^2 - \omega_0^2)^2 - \omega_0^2 (1 + q_0^2 - \omega_0^2)^2}} & 1 + \frac{q_0^2 (1 + q_0^2 - \omega_0^2) \sin^2 \theta}{(q_0^2 - \omega_0^2)^2 \omega_{c0}^2 - \omega_0^2 (1 + q_0^2 - \omega_0^2)^2} \end{pmatrix} \phi_n^T \equiv H \phi_n^T = 0, \quad (17)$$

where $\phi_n = (\phi_0, n_{10})$, and H is a 2×2 Hermitian matrix. We ignored the term $v_{F0}^2 (q_0^2 - \omega_0^2)$ because $|v_{F0}^2 (q_0^2 - \omega_0^2)| \ll 1$.

The above equation shows that the "effective" coupling between the axion and PP in the system is not g but g_n , meaning that the hybridization between the axion and PP, and therefore, their spectra are mainly determined by g_n (and ω_{c0} , $\omega_{\phi 0}$). This is an important result. Under ordinary conditions, g is considerably small; however, considering the obtained results, one can tune the parameters to enhance the coupling g_n . To determine how to enhance the coupling, we wrote the enlargement factor as $A_m = e \pi c (\frac{\epsilon_0 \hbar c}{e^2})^{3/2} \frac{B_0 d}{E_F} \equiv 3.39 \times 10^8 \times \frac{B_0 (T) d (cm)}{E_F (eV)}$. Therefore, one can increase A_m by increasing the external background magnetic field and layer distances (it is important to note the requirement that d should be far smaller than the wave length) or decreasing carrier concentration (or equivalently, gate voltage).

As expected, in the decoupled case, *i.e.* $g_n = 0$, there are four modes: one corresponds to the axion and the other three correspond to the PP modes. In the coupled case, the axion mode hybridizes with three PP modes. If $\omega_{\phi 0} \geq 1$, the axion mode mainly hybridizes with the high and optical mode. In this study, we focus on the ultralight axion, $\omega_{\phi 0} \ll 1$. In this case the axion mainly hybridizes with the acoustic mode, particularly in the long wave limit.

We nominate the coupled axion/the acoustic mode as the axion hybridization state/acoustic hybridization state (AXHS/ACHS) as AXHS/ACHS also contains PP/axion constitution owing to the hybridization and AXHS/ACHS are pure axion/acoustic PP states when $g_n \rightarrow 0$.

The results of AXHS and ACHS are shown in Fig. 3 (a), where $\omega_{\phi 0} = 0.1$, $\omega_{c0} = 0.5$ and $\theta = \pi/4$. For the decoupled case, $g_n = 0$, the AXHS dispersion is $\omega_{ax0} = \sqrt{\omega_{\phi 0}^2 + q_0^2}$ and the ACHS dispersion is the same as in Fig. 2, *i.e.*, $\omega_{a0} \simeq q_0 \sin \theta$ in the long wave limit. However, in the coupled case, for instance, $g_n = 0.3$, the hybridization between the axion and acoustic PP occurs. The AXHS increases and the ACHS decreases owing to the hybridization. Therefore, the gap between them becomes larger. Additionally, in the long-wave limit, the ratio between ω_{a0} and q_0 , $r(g_n) \equiv \lim_{q_0 \rightarrow 0} \frac{\omega_{a0}}{q_0}$, should be smaller than $\sin \theta$, as shown in Fig. 3(a). To verify the result, we also list $r(g_n)$ at different angles for cases $g_n = 0, 0.03, 0.1, 0.3$ in Figs. 3(b,c), which show that as g_n deviates from zero, the ratio deviates from the uncoupled case $r(g_n = 0) = \sin \theta$. Furthermore, the smaller ω_{ϕ} is, the more significant the deviation. Fig. 3(c) exemplifies that the deviation is significant even when $g_n = 0.03$ at the case $\omega_{\phi 0} = 0.04$. In the presence of hybridization, both ACHS and AXHS spectra can be detected using common photoelectric methods in the laboratory. Therefore, it is a suitable method to measure the deviation of $r(g_n)$ to judge the presence or absence of axions in the universe. As the measurement is independent of resonance, the detectable axion mass range is broad. In particular, the measurement becomes more sensitive as the axion mass decreases.

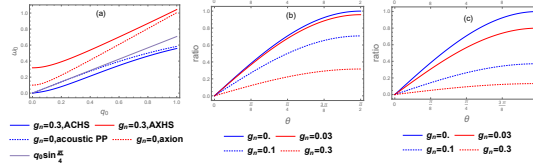


Figure 3: Dispersion relations of AXHS and ACHS (a) and ratios between ω_{a0} and q_0 at different angle in the long wave limit. Besides $\omega_{c0} = 0.5$, we also set $\theta = \frac{\pi}{4}$ (a), $\omega_{\phi 0} = 0.1$ (b), and $\omega_{\phi 0} = 0.04$ (c). In (b,c) ratio at the decoupled case is just $r(g_n = 0) = \sin \theta$.

Furthermore, it is important to study the influence of the background magnetic field on the AXHS spectrum or ACHS spectrum, which was shown in Fig. 4. The AXHS spectrum is insignificantly affected by ω_{c0} and the ACHS spectrum is mildly affected when g_n remains constant. The results revealed that the impact of background magnetic field on the AXHS spectrum is mostly due to g_n and not ω_{c0} ; meanwhile, both ω_{c0} and g_n influence the ACHS spectrum.

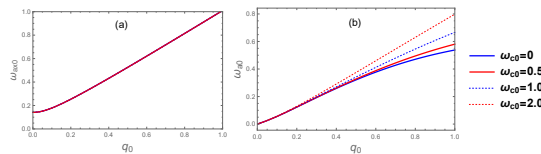


Figure 4: Dispersion relations of AXHS (a) and ACHS (b) at different background magnetic field (ω_{c0}). Here we set $\omega_{\phi 0} = 0.1$, $\theta = \frac{\pi}{4}$ and $g_n = 0.1$.

4 Conclusions

We investigated and discussed the coupling between the axion and PP as well as the spectrum of AXHS and ACHS in a doped graphene periodic structure. The discussion highlighted that the effective coupling between the axion and PP, g_n , depends on parameters such as carrier concentration, interlayer distance, and background magnetic field. Accordingly, these parameters can be tuned to enhance effective coupling.

We further studied the hybridization between the axion and PP, particularly, acoustic PP stemming from the effective coupling g_n . The hybridization modified the dispersion relations of AXHS and ACHS efficiently. An observable, $r(g_n)$, was proposed to detect axions accordingly. As long as the axion mass is sufficiently small, the deviation of $r(g_n)$ from uncoupled behavior $\sin \theta$ is significant even when the effective coupling is not large.

With the use of the above two developments, we believe it is possible to detect axions in the laboratory. Furthermore, as the measurement is independent on the resonance phenomenon, the detectable range of axion mass is wide. Our proposed system provides an easy-to-realize and sensitive platform for detecting axions in the universe.

References

- [1] R.D. Peccei and H.R. Quinn, *CP conservation in the presence of instantons*, *Phys. Rev. Lett.* **38**(1977) 1440
- [2] S. Weinberg, *A new light boson?*, *Phys. Rev. Lett.* **40** (1978) 223.
- [3] S. Sen and L. Sivertsen, *Electromagnetic radiation from axion condensates in a time dependent magnetic field*, *J. High Energ. Phys.* **2022**, 192(2022).
- [4] J.E. Kim, *Light pseudoscalars, particle physics and cosmology*, *Phys. Rept.* **150** 1(1987).
- [5] G.G. Raffelt, *Astrophysical methods to constrain axions and other novel particle phenomena*, *Phys. Rept.* **198** 1 (1990).
- [6] L.D. Duffy and K. van Bibber, *Axions as dark matter particles*, *New J. Phys.* **11** 105008(2009).
- [7] A.S. Sakharov, D.D. Sokoloff and M.Y. Khlopov, *Large scale modulation of the distribution of coherent oscillations of a primordial axion field in the universe*, *Phys. Atom. Nucl.* **59** 1005(1996).
- [8] M.Y. Khlopov, A.S. Sakharov and D.D. Sokoloff, *The nonlinear modulation of the density distribution in standard axionic CDM and its cosmological impact*, *Nucl. Phys. B Proc. Suppl.* **72** 105(1999).
- [9] S. J. Asztalos, G. Carosi, C. Hagmann, D. Kinion, K. van Bibber, M. Hotz, L. J. Rosenberg, G. Rybka, J. Hoskins, J. Hwang, P. Sikivie, D. B. Tanner, R. Bradley, and J. Clarke, *SQUID-Based microwave cavity search for dark-matter axions*, *Phys. Rev. Lett.* **104** 041301(2010).
- [10] K. M. Backes, D. A. Palken, S. Al Kenany, B. M. Brubaker, S. B. Cahn, A. Droster, Gene C. Hilton, Sumita Ghosh, H. Jackson, S. K. Lamoreaux, A. F. Leder, K. W. Lehnert, S. M. Lewis, M. Malnou, R. H. Maruyama, N. M. Rapidis, M. Simanovskaia, Sukhman Singh, D. H. Speller, I. Urdinaran, Leila R. Vale, E. C. van Assendelft, K. van Bibber and H. Wang, *A quantum enhanced search for dark matter axions*, *Nature*, **590** 238-242(2021).
- [11] J. Wang, X. Bi and P. Yin, *Detecting axion dark matter through the radio signal from Omega Centauri*, *Phys. Rev.* **D104** 103015(2021).
- [12] ADMX Collaboration, *Extended search for the invisible axion with the axion dark matter experiment*, *Phys. Rev. Lett.* **124** 101303(2020).
- [13] M. Buschmann, J.W. Foster and B.R. Safdi, *Early-Universe simulations of the cosmological axion*, *Phys. Rev. Lett.* **124** 161103(2020).
- [14] K. Nagano, T. Fujita, Y. Michimura and I. Obata, *Axion dark matter search with interferometric gravitational wave detectors*, *Phys. Rev. Lett.* **123**, 111301(2019).
- [15] M. Malnou, D.A. Palken, B.M. Brubaker, Leila R. Vale, Gene C. Hilton, and K.W. Lehnert, *Squeezed vacuum used to accelerate the search for a weak classical signal*, *Phys. Rev.* **X9** 021023(2019)
- [16] H. Tercas, J.D. Rodrigues and J.T. Mendonca, *Axion-plasmon polaritons in strongly magnetized plasmas*, *Phys. Rev. Lett.* **120** 181803(2018).
- [17] J.T. Mendonca, J.D. Rodrigues and H. Tercas, *Axion production in unstable magnetized plasmas*, *Phys. Rev.* **D101** 051701(2020).
- [18] K. Taguchi, T. Imaeda, T. Hajiri, T. Shiraishi, Y. Tanaka, N. Kitajima and T. Naka, *Electromagnetic effects induced by time-dependent axion field*, *Phys. Rev.* **B97** 214409(2018).
- [19] S. Das, P. Jain, J.P. Palston and R. Saha, *The dynamical mixing of light and pseudoscalar fields*, *J. Phys.* **70(3)** 439-456(2008)

- [20] C.M. Donohue, S. Gardner and W. Korsch, *LC circuits for the direct detection of ultralight dark matter candidates*, arXiv:hep-ph/2109.08163(2021).
- [21] R. Grimaudo, D. Valenti, B. Spagnolo, G. Filatrella and C. Guarcello, *Josephson junction-based axion detection through resonant activation*, *Phys. Rev.* **D105** 033007(2022).
- [22] XMASS Collaboration, *Search for dark matter in the form of hidden photons and axion-like particles in the XMASS detector*, *Phys. Lett.* **B787** 153-158(2018).
- [23] QUAX Collaboration, *Axion search with a quantum-limited ferromagnetic haloscope*, *Phys. Rev. Lett.* **124** 171801(2020).
- [24] E. Berkowitz, M. I. Buchoff and E. Rinaldi, *Lattice QCD input for axion cosmology*, *Phys. Rev.* **D92** 034507(2015).
- [25] MADMAX Working Group, *Dielectric haloscopes: a new way to detect axion dark matter*, *Phys. Rev. Lett.* **118** 091801(2017).
- [26] N. V. Mikheev, G. Raffelt, L. A. Vassilevskaya, *Axion emission by magnetic-field induced conversion of longitudinal plasmons*, *Phys. Rev.* **D58** 055008(1998).
- [27] M. Lawson, A.J. Millar, M. Pancaldi, E. Vitagliano and F. Wilczek, *Tunable axion plasma haloscopes*, *Phys. Rev. Lett.* **123** 141802(2019).
- [28] A.J. Chaves, N.M.R. Peres, G. Smirnov and N.A. Mortensen, *Hydrodynamic model approach to the formation of plasmonic wakes in graphene*. *Phys. Rev.* **B96**, 195438(2017).
- [29] D. Liu, Z. Xu, N. Ma and S. Zhang, *Graphene modulated by external fields: a nonresonant left-handed metamaterial*. *Appl. Phys.* **A106**, 949-954(2012).
- [30] D. Liu, L. Wang, Y. Fan, L. Zhang, X. Jiang and X. Zhao, *A scheme to excite transverse electric graphene plasmon polariton with positive value of imaginary part of conductivity*. *AIP Adv.* **11**, 055010(2021).
- [31] X. He, J. Tao and B. Meng, *Analysis of graphene TE surface plasmons in the terahertz regime*. *Nanotech.* **24**, 345203(2013).